Supporting Information for

“Magnetic Skyrmion Arrangement Tuning by Surface Acoustic Waves”

Shouzhe Dong[1,2], Changqing Guo[1,2], Ke Xu[1,2], Chen Liang[1,2], Chengchao Hu[3], Letao Yang[1,2], Jing Wang[1,2] and Houbing Huang[1,2]*

[1] School of Materials Science and Engineering, Beijing Institute of Technology, Beijing 100081, PR China

[2] School of Interdisciplinary Science, Beijing Institute of Technology, Beijing, 100081, PR China

3 Aerospace and Informatics Domain， Beijing Institute of Technology， Zhuhai，519088， PR China

*Corresponding author: hbhuang@bit.edu.cn (Houbing Huang)

This PDF file includes:

Methods

Figures S1-S14

Methods

Phase field simulation: In this phase-field model, the magnetization field $\boldsymbol{M} = M_s(m_1, m_2, m_3)$ is used to characterize the magnetic domain structure, where m_i (i = x, y, z) represents the components of the unit magnetization vector m along the local crystallographic axes. The saturation magnetization is denoted by M_s. The evolution of the magnetization configuration is governed by the Landau-Lifshitz-Gilbert (LLG) equation, which captures the time-dependent dynamics of the magnetic domains[1,2]:

$$(1+\alpha^2)\frac{\partial \boldsymbol{M}}{\partial t} = -\gamma_0 \boldsymbol{M} \times \boldsymbol{H}_{\text{eff}} - \frac{\gamma_0 \alpha}{M_s} \boldsymbol{M} \times (\boldsymbol{M} \times \boldsymbol{H}_{\text{eff}}) \text{\\* MERGEFORMAT (1)}$$

In the formula 1, α is the damping constant, γ_0 is the gyromagnetic ratio, and $\boldsymbol{H}_{\text{eff}}$ is the effective magnetic field, which can be described by the following equation:

$$\boldsymbol{H}_{\text{eff}} = \frac{-1}{\mu_0 M_{\text{s}}} \frac{\delta F_{\text{tot}}}{\delta \boldsymbol{m}} \qquad \text{\\* MERGEFORMAT (2)}$$

In the formula 2, μ_0 and F_{tot} denote vacuum permeability and total free energy denisty, respectively. The total free energy density can be written as:

$$F_{tot} = F_{\text{anis}} + F_{\text{demag}} + F_{\text{zeem}} + F_{\text{exch}} + F_{\text{dmi}} + F_{\text{elas}} + F_{\text{mel}} + F_{\text{kin}} \text{\\* MERGEFORMAT (3)}$$

In the formula 3, F_{anis}, F_{zeem}, F_{demag}, F_{exch}, F_{dmi}, F_{elas}, F_{mel} and F_{kin} are the magnetocrystalline anisotropy energy density, zeeman energy density, demagnetization energy density, exchange energy density, Dzyaloshinskii-Moriya interaction (DMI) energy density, elastic energy density and magnetoelastic coupling energy density and kinetic energy density, respectively. The volume of the anisotropy energy density is given by[3]

$$F_{\mathrm{anis}} = K_1(1-{m_3}^2) + K_2(1-{m_3}^2)^2$$ * MERGEFORMAT (4)

In the formula 4, m_3 denotes the M_z component, where K_1 and K_2 are the uniaxial anisotropy constants. The demagnetization energy density of a system can be written as:

$$F_{\mathrm{demag}} = -\frac{1}{2}\mu_0 M_{\mathrm{s}} \boldsymbol{H}_{dem} \cdot \boldsymbol{m}$$ * MERGEFORMAT (5)

In the formula 5, $\boldsymbol{H}_{\mathrm{dem}}$ is the demagnetization field, determined by the long-range interaction among the magnetic moments in the system, which is obtained at each evolution step by solving the magnetostatic equilibrium equation:

$$\nabla \cdot (\boldsymbol{H}_{\mathrm{dem}} + \boldsymbol{M}) = 0$$ * MERGEFORMAT (6)

The Zeeman energy density, also known as the external magnetic field energy density, which can be written as:

$$F_{zeem} = -\mu_0 M_{\mathrm{s}} \boldsymbol{H}_{ext} \cdot \boldsymbol{m}$$ * MERGEFORMAT (7)

In the formula 7, $\boldsymbol{H}_{\mathrm{ext}}$ is the external field.

The exchange energy density is determined by the spatial variation of the magnetization orientation and can be described as:

$$F_{\mathrm{exch}} = -A(\nabla \boldsymbol{m})^2$$ * MERGEFORMAT (8)

In the formula 8, A is employed to describe the nearest-neighbor interaction coefficients between two spins. The DMI energy density is given by:

$$F_{dmi} = D(m_3 \nabla \cdot \boldsymbol{m} - \boldsymbol{m} \cdot \nabla m_3)$$ * MERGEFORMAT (9)

In the formula 9, D represents the homogenous effective DMI constant. The elastic energy density can be described as:

$$F_{\text{elas}} = \frac{1}{2}\sum_{i,j,k,l} c_{ijkl}\varepsilon_{\text{kl}}\varepsilon_{ij}$$
* MERGEFORMAT (10)

where ε_{ij} and c_{ijkl} are the total strain components and the stiffness constants, (i, j, k, l = 1, 2, 3). The magnetoelastic coupling energy density can be described as[4–6]:

$$F_{\text{mel}} = B_1\sum_i m_i^2\varepsilon_{ii} + B_2\sum_{\text{i}\neq\text{j}} m_i m_j\varepsilon_{ij}$$
* MERGEFORMAT (11)

In the formula 11, B_1 and B_2, the magnetoelastic coupling constants, are related to the magnetostriction constants λ_{100} and λ_{111} through the following relationships[7,8]:

$$B_1 = -\tfrac{3}{2}\lambda_{100}(c_{11} - c_{12}),\ B_2 = -3\lambda_{111}c_{44}$$
* MERGEFORMAT (12)

The strain matrix is given by:

$$\begin{pmatrix} \varepsilon_{xx} & \varepsilon_{xy} & \varepsilon_{xz} \\ \varepsilon_{yx} & \varepsilon_{yy} & \varepsilon_{yz} \\ \varepsilon_{zx} & \varepsilon_{zy} & \varepsilon_{zz} \end{pmatrix} = \begin{pmatrix} \varepsilon_{rr}^s \frac{x^2}{r^2} cos\, kr\, cos\, wt & 0 & -\varepsilon_{rz}^s \frac{x^2}{r^2} sin\, kr\, cos\, wt \\ 0 & \varepsilon_{rr}^s \frac{y^2}{r^2} cos\, kr\, cos\, wt & -\varepsilon_{rz}^s \frac{y^2}{r^2} sin\, kr\, cos\, wt \\ -\varepsilon_{rz}^s \frac{x^2}{r^2} sin\, kr\, cos\, wt & -\varepsilon_{rz}^s \frac{y^2}{r^2} sin\, kr\, cos\, wt & \varepsilon_{zz}^s\, cos\, kr\, cos\, wt \end{pmatrix}$$
* MERGEFORMA

In the formula 13, $r = \sqrt{x^2 + y^2}$ is the radial coordinate, x and y represents the horizontal and vertical distances from the center of the nanoisland. k and ω are the wave vector and the angular frequency of the SAW, respectively. The radial strain $\varepsilon_{rr} = \varepsilon_{xx} + \varepsilon_{yy}$. ε_{rr}^s ε_{rz}^s, and ε_{zz}^s represent some coefficients of the matrix components. The radial sinusoidal strain oscillates exclusively along the radial direction, and points on the same circumference exhibit no tangential displacement, thus, the shear strain ε_{xy} is set to zero. During the calculations, the strain is assumed to be uniformly distributed along the azimuthal direction (i.e., exhibiting circumferential symmetry).

The kinetic energy density can be expressed as[9]

$$F_{\text{kin}} = \frac{\rho \left\| \frac{\partial \boldsymbol{u}}{\partial t} \right\|^2}{2} \quad \text{* MERGEFORMAT (14)}$$

In the formula 14, ρ is the mass density and $\boldsymbol{u}$ the mechanical displacement. Assuming that the elastic equilibrium condition holds at each evolution step, the elastodynamic equation of motion is given by

$$\rho \frac{\partial^2 \mathbf{u}}{\partial t^2} + \eta \frac{\partial \mathbf{u}}{\partial t} = \nabla \cdot \sigma + f_{\text{tot}} \quad \text{* MERGEFORMAT (15)}$$

In the formula 15, η is a phenomenological damping parameter and f_{tot} is the total body force acting on the material. The description of key SAW and strain parameters is as follows：

B_1 (J/m) [6,10,11]	B_2 (J/m) [6,10,11]	Wavelength λ (nm) (2π/k) [10,11]	Frequency f (GHz) (w/2π) [10,12]	ε^{s}_{rr} [6,10,11]
1×10^7	1×10^7	30 ~ 60	0.17	0.09 ~ 0.128
ε^{s}_{zz} [6,10,11]	ε^{s}_{rz} [6,10,11]	Crystal types of $LiNbO_3$ [6,10–14]	Propagation velocity of SAW (m/s) [6,10,11,13]	Modes of SAW[6,10,11]
0.009 ~ 0.0128	0.0032 ~ 0.0064	Y-cut	3765	Rayleigh wave
Mass Density ρ (kg/m^3)	Damping parameter η	λ_{100}[6,10,11]	λ_{111}[6,10,11]	c_{11} (GPa) [6,10,11]
8×10^3	0	-4.6×10^{-5}	-4.6×10^{-5}	309
c_{12} (GPa) [6,10,11]	c_{44} (GPa) [6,10,11]			
165	72			

Table 1 Description of Key SAWs and Strain Parameters

Neural network:

Dataset: The data comes from the modified CIFAR-10 dataset. The CIFAR-10 dataset includes 60000 color images with a size of 32×32-pixels (50000 for training and 10000 for testing). The color of each pixel is represented by three channels, and the image is divided into 10 different classes.

Weight: The measured magnetization component M_z is first normalized to the range of -1 to +1, and each synaptic weight to this interval. In the implementation, weights are stored as 32-bit floating-point numbers, and during forward propagation, each weight is replaced by the closest corresponding magnetization component value. After computing the loss, gradients are back-propagated and weights are updated for the next forward pass. To ensure correct gradient computation despite the non-differentiable weight-replacement operation, a straight-through estimator (STE) is employed to approximate gradients through the quantization process.

Training details: Our experiments are implemented using the PyTorch framework. Both networks are trained for 200 epochs with a batch size of 128 on an NVIDIA GeForce RTX 4070Ti GPU, employing the cross-entropy loss and the SGD optimizer (momentum = 0.9, weight decay = 5×10^{-4}). The initial learning rate is set to 0.1 and is halved at the 100th and 160th epochs.

Supplementary Note 1: The size of skyrmions under an out-of-plane (+z) magnetic field of 500 mT

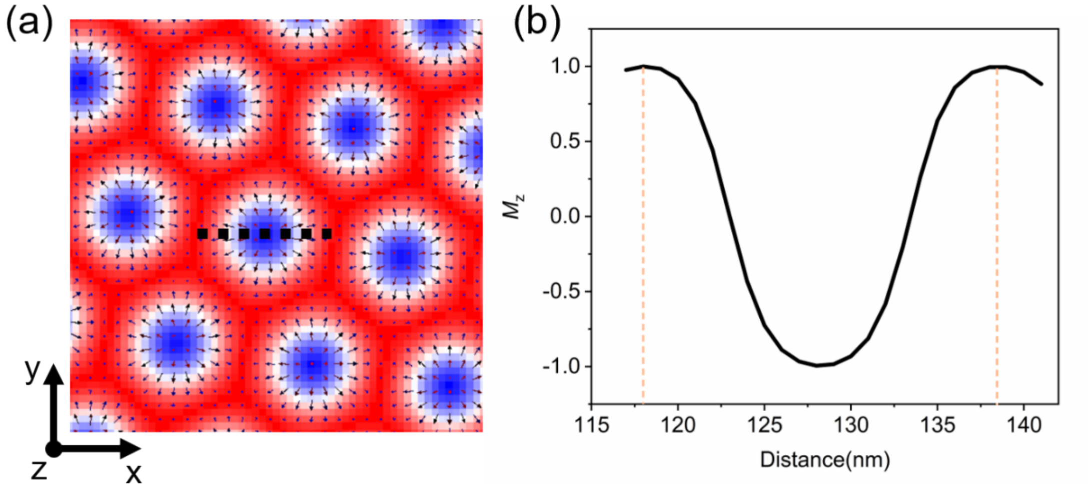

Fig. S1 Determination of skyrmion dimensions. (a) Local distribution of the metastable domain configuration under an out-of-plane (+z) external field of 500 mT without SAW excitation. (b) Variation of the M_z component along the black dashed line.

Supplementary Note 2: Effect of DMI strength on the skyrmion rearrangement behavior under SAW excitation.

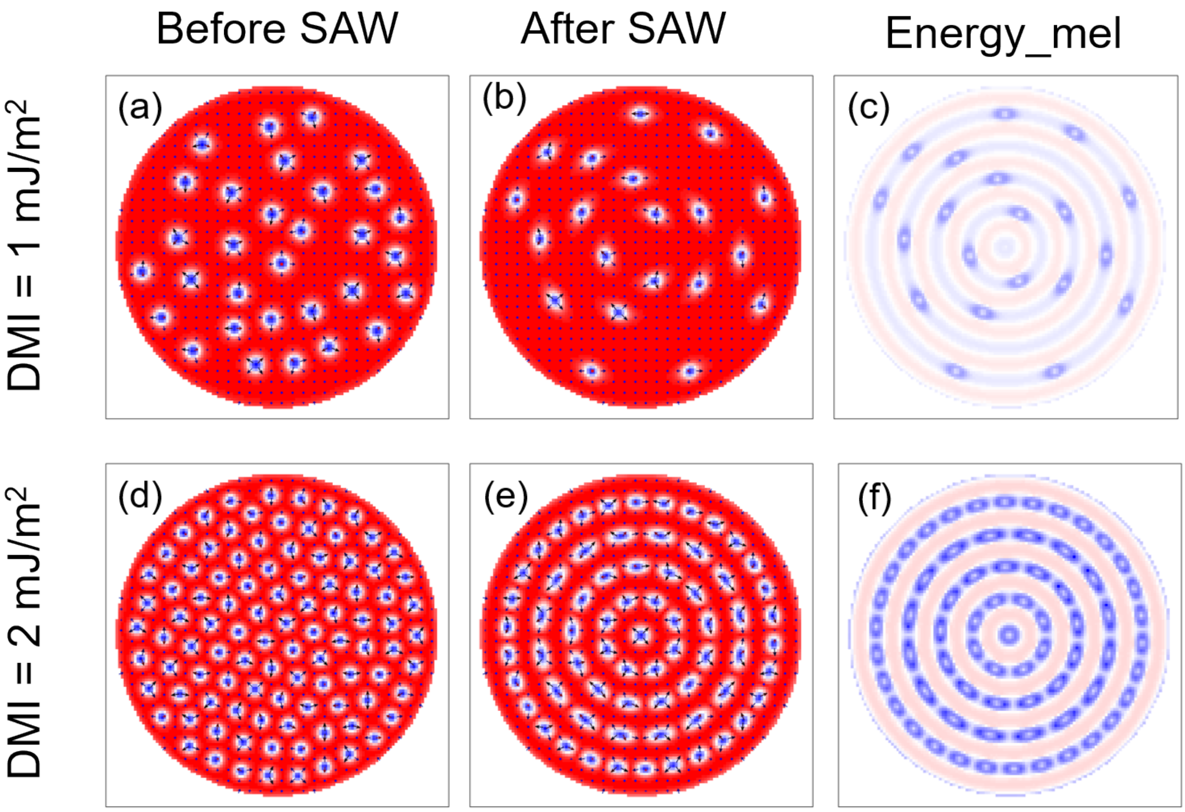

Fig. S2 Effect of DMI strength on the skyrmion rearrangement behavior under SAW excitation. (a)–(c) Skyrmion configurations before and after SAW excitation, and the corresponding magnetoelastic energy density distribution at t = 9.36 ns, for D = 1 mJ/m^2. **d–f** The same sequence for D = 2 mJ/m^2.

Supplementary Note 3: Skyrmion rearrangement induced by SAW excitation with a radial strain amplitude of 0.001 under different external magnetic fields.

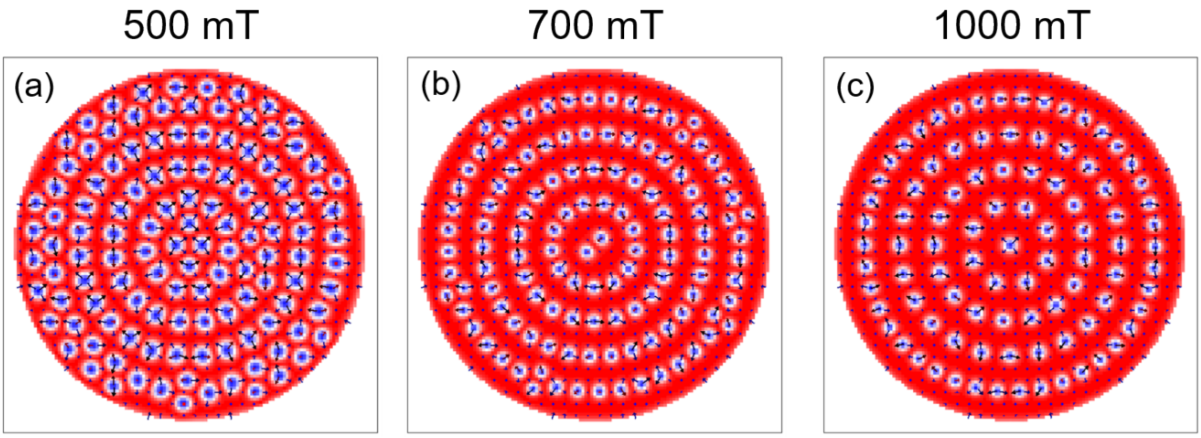

Fig. S3 Skyrmion rearrangement induced by SAWs excitation with a radial strain amplitude of 0.001 under external magnetic fields of (a) 500 mT, (b) 600 mT and (c) 1000 mT.

Supplementary Note 4: Skyrmion rearrangement induced by SAW excitation under different temperature.

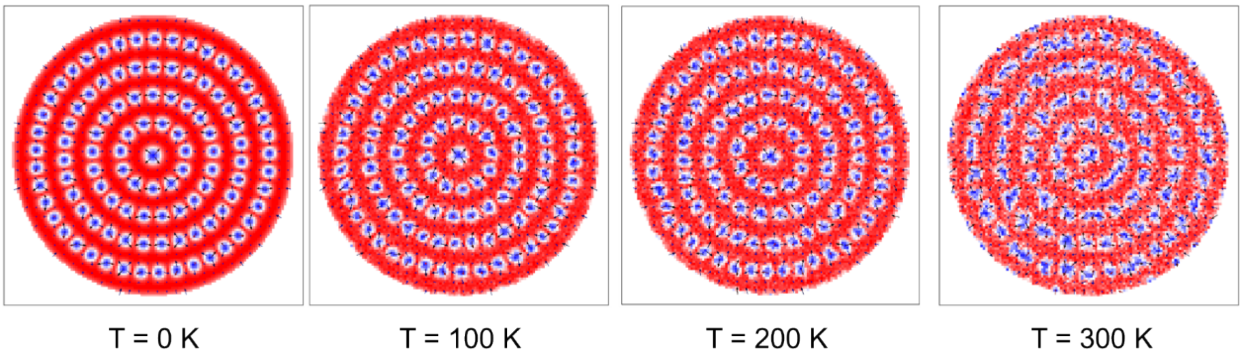

Fig. S4 Effect of temperature on SAW-driven skyrmion rearrangement. Snapshots are taken at t = 9.36 ns under an external field of 500 mT and a strain amplitude of 0.128 for various temperatures.

Supplementary Note 5: Strain distribution of $[Co/Pd]_n$ multilayer nano-islands at t = 9.36 ns

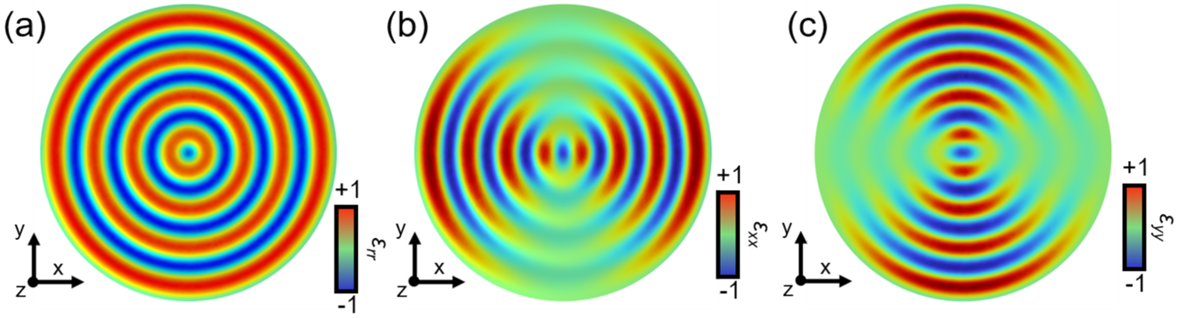

Fig. S5 (a) ε_{rr}, (b) ε_{xx} and (c) ε_{yy} strain distribution of $[Co/Pd]_n$ multilayer nano-islands at t = 9.36 ns.

Supplementary Note 6: Temporal evolution of the energy density under nonuniform strain

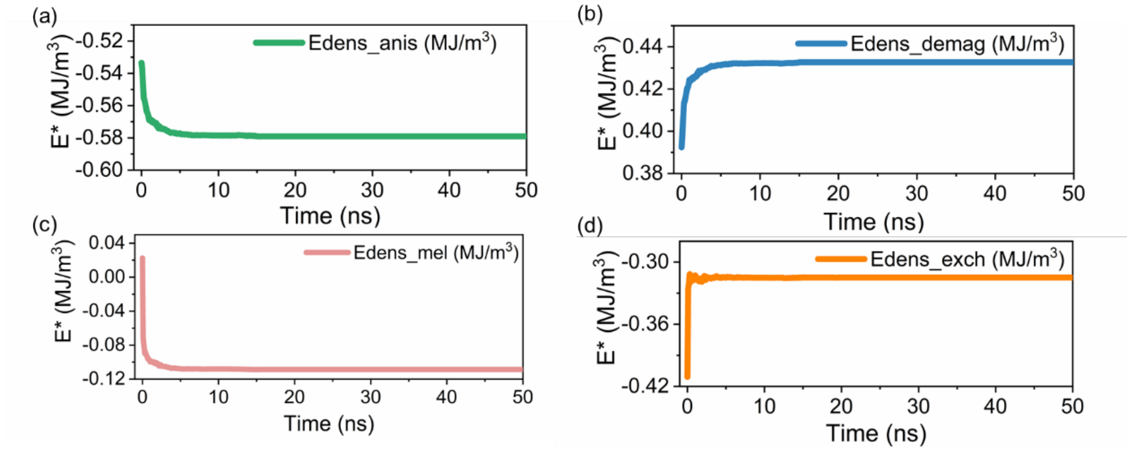

Fig. S6 Temporal evolution of the energy density under nonuniform strain: (a) magnetocrystalline anisotropy energy density, (b) demagnetization energy density, (c) magnetoelastic coupling energy density, and (d) exchange energy density.

Supplementary Note 7: Temporal evolution of the energy density changes relative to their initial states under nonuniform strain

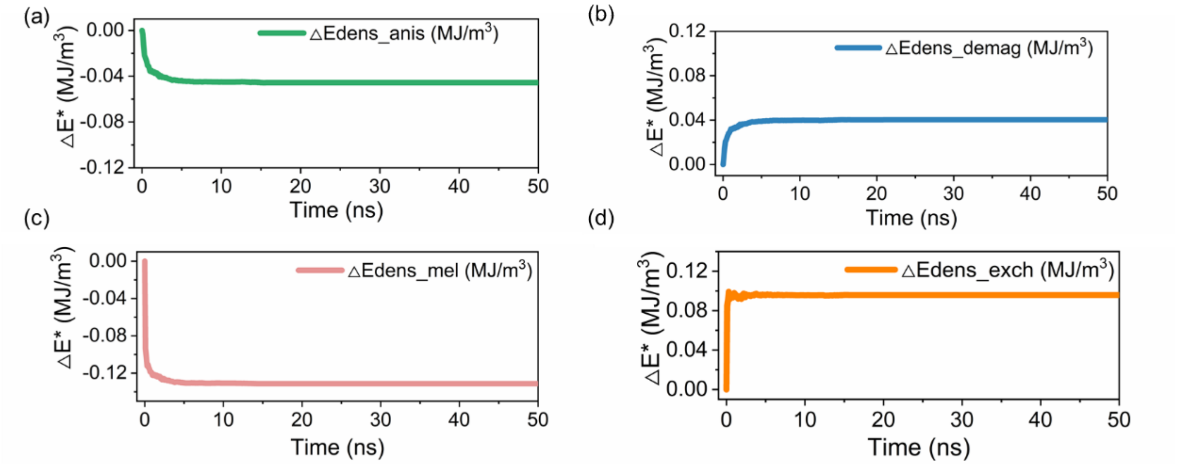

Fig. S7 Temporal evolution of the energy density changes relative to their initial states under nonuniform strain: (a) magnetocrystalline anisotropy energy density, (b) demagnetization energy density, (c) magnetoelastic coupling energy density, and (d) exchange energy density.

Supplementary Note 8: Dynamic evolution of skyrmions under sinusoidal nonuniform strain and sinusoidal nonuniform K_1, respectively.

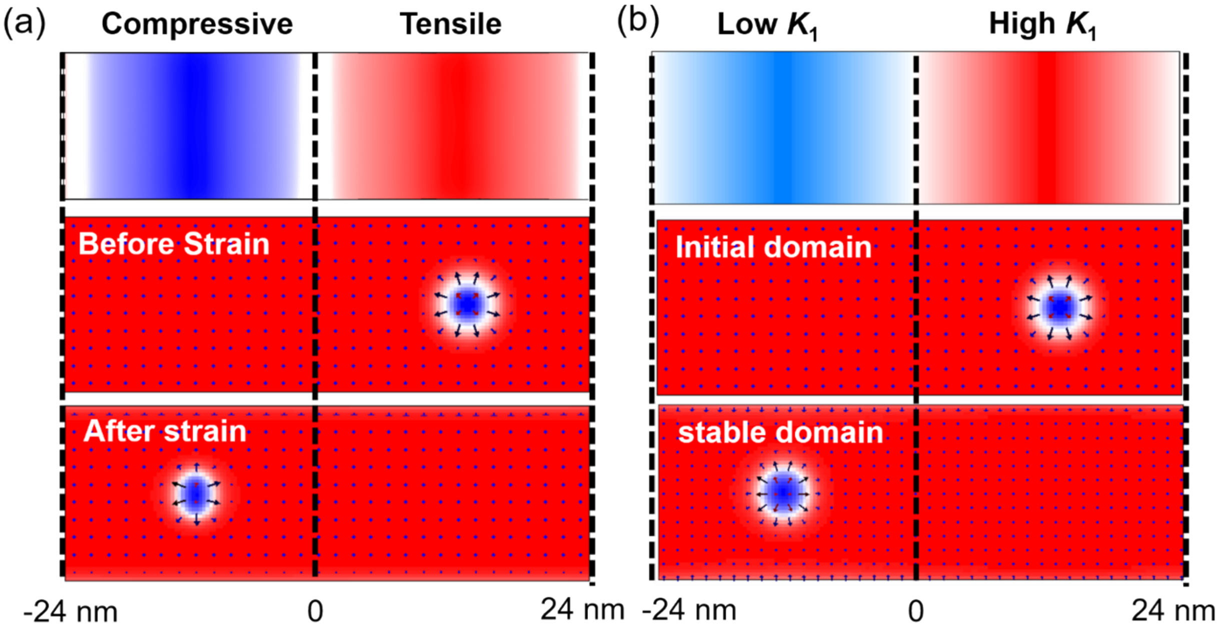

Fig. S8 Dynamic evolution of skyrmions under (a) sinusoidal nonuniform strain and (b) sinusoidal nonuniform K_1, respectively. $K_1 = K_0 + 0.2K_0 \times \cos(2\pi x / (48 \times 10^{-9}))$, where $K_0 = 1.2 \times 10^6$ J/m^3 and x represents the horizontal distance from the center.

Supplementary Note 9: Rearrangement Behavior 1: Enter the inner adjacent anti-nodes of the wave.

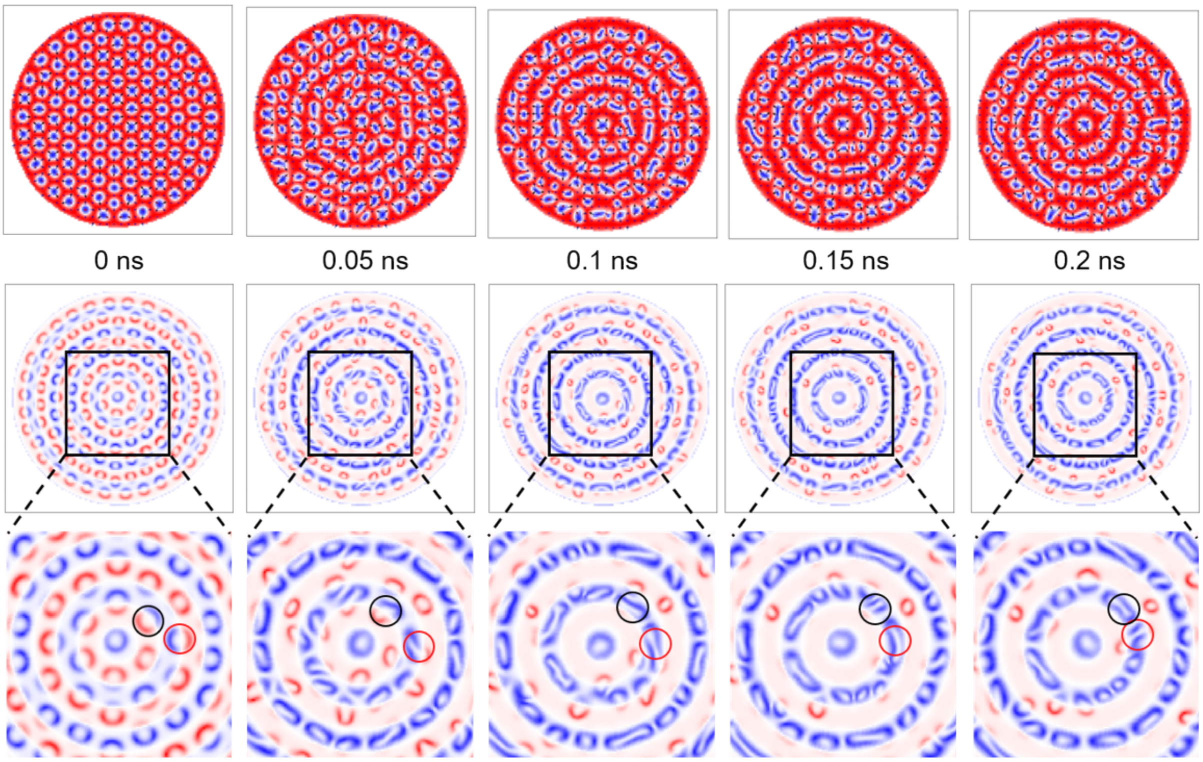

Fig. S9 Simulate the movement behavior of skyrmions that migrate towards the anti-nodes of the inner neighboring waves following the nonuniform strain distribution.

Supplementary Note 10: Rearrangement Behavior 2: Enter the outer adjacent anti-nodes of the wave.

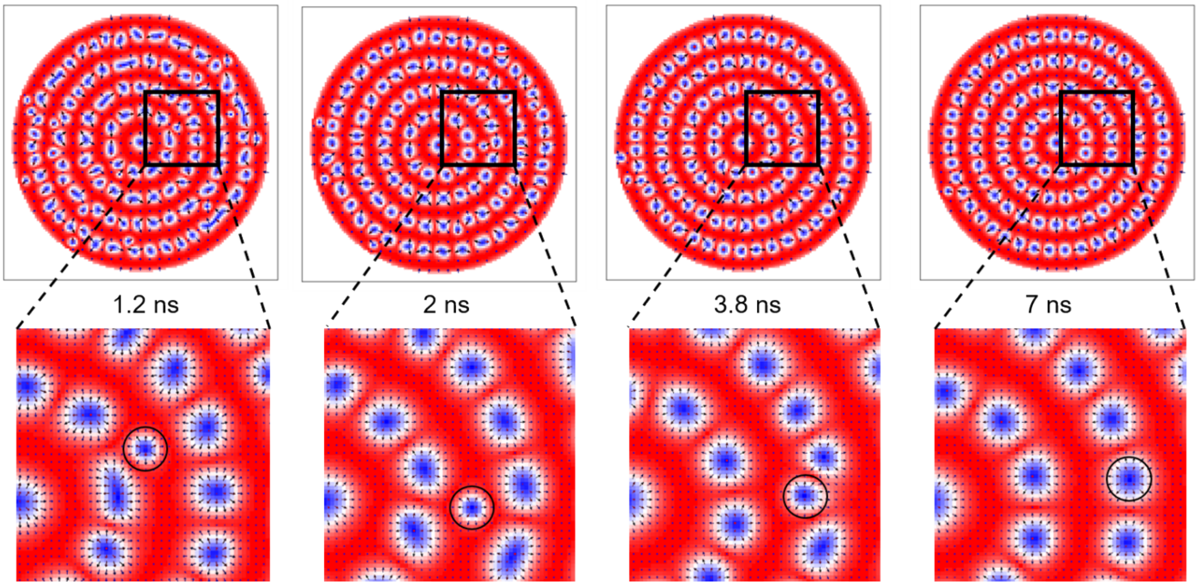

Fig. S10 Simulate the movement behavior of skyrmions towards the anti-nodes of the outer neighboring waves following the nonuniform strain distribution.

Supplementary Note 11: Rearrangement Behavior 3: Annihilate at the boundary of nano-islands

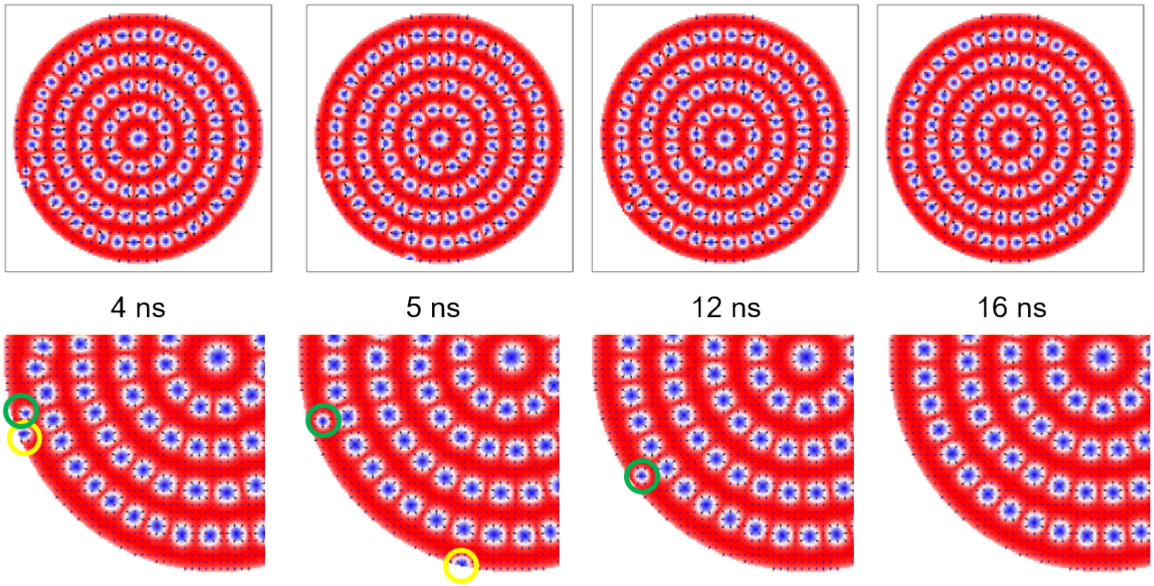

Fig. S11 Simulate the annihilation behavior of skyrmions at the boundary following the nonuniform strain distribution.

Supplementary Note 12: Phase diagrams of metastable domain structures under different external fields, amplitude and wavelength.

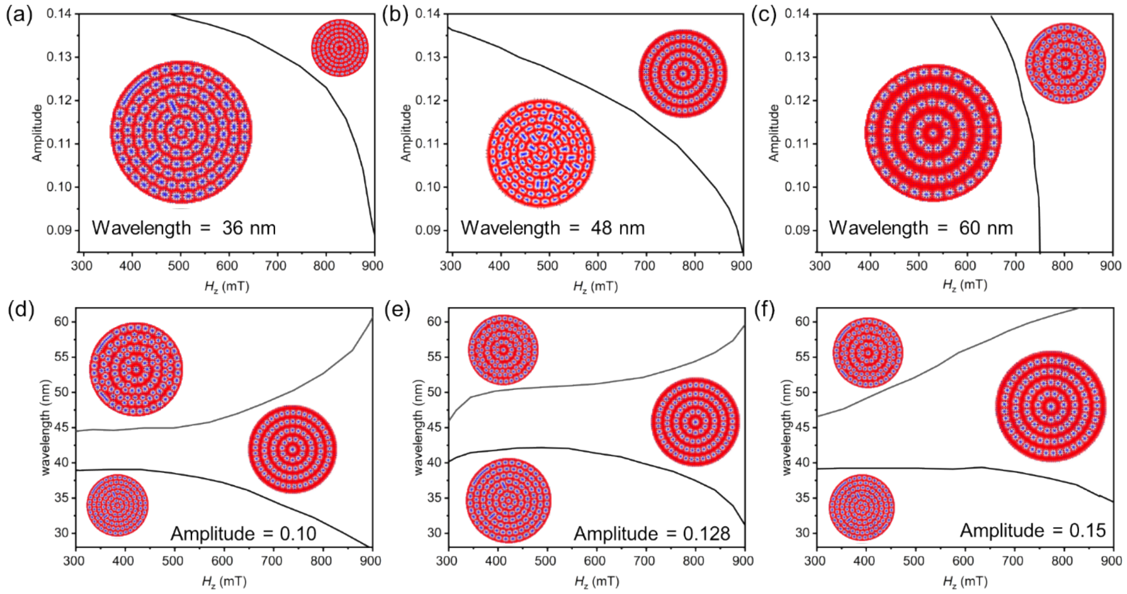

Fig. S12 Phase diagrams of metastable domain structures. (a)–(c) Domain patterns as a function of external magnetic field and strain amplitude for (a) wavelength = 36 nm, (b) wavelength = 48 nm and (c) wavelength = 60 nm. (d)–(f) Domain patterns as a function of external magnetic field and SAW wavelength for strain amplitudes of (d) ε_{rr} = 0.1, (e) ε_{rr} = 0.128 and (f) ε_{rr} = 0.15. ε_{rr} represents the radial strain

Supplementary Note 13: Snapshots of domain structures at t = 9/4 T under different SAW frequencies.

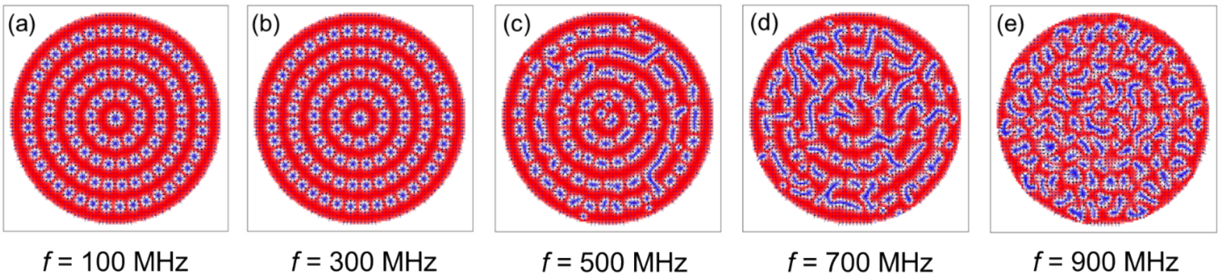

Fig. S13 Snapshots of domain structures at t = 9/4 T under different SAW frequencies. (a)–(e) Simulated magnetization configurations for frequencies of (a) *f* = 100 MHz, (b) *f* = 300 MHz, (c) *f* = 500 MHz, (d) *f* = 700 MHz and (e) *f* = 900 MHz.

Supplementary Note 14: Evolution of skyrmion distribution during pulsed SAW excitation.

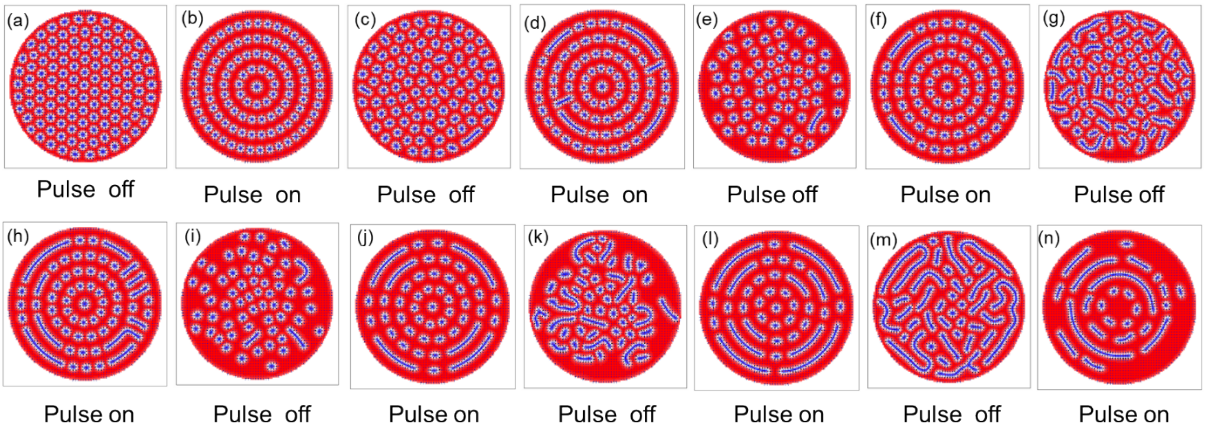

Fig. S14 Evolution of skyrmion distribution during pulsed SAW excitation. The pulse frequency is 170 MHz, with a pulse duration of 29.4 ns (approximately 5 cycles) and an inter-pulse interval of 50 ns.

Supplementary Information References

1 J. M. Hu, G. Sheng, J. X. Zhang, C. W. Nan and L. Q. Chen, *Appl. Phys. Lett.*, 2011, **98**, 112505.

2 J. X. Zhang and L. Q. Chen, *Acta Mater.*, 2005, **53**, 2845–2855.

3 J. M. Hu, T. N. Yang and L. Q. Chen, *Npj Comput. Mater.*, 2018, **4**, 62.

4 S. Datta, *Surface Acoustic Wave Devices*, Englewood Cliffs, N.J, 1986.

5 R. Sasaki, Y. Nii, Y. Iguchi and Y. Onose, *Phys. Rev. B*, 2017, **95**, 020407.

6 J. T. Shuai, M. N. Ali, L. Lopez-Diaz, J. E. Cunningham and T. A. Moore, *Appl. Phys. Lett.*, 2022, **120**, 252402.

7 S. Chikazumi, *Physics of Ferromagnetism*, Oxford University Press, Oxford, 2nd edition., 2009.

8 Y. Li, C. B. Zhao, W. Zhang, A. Hoffmann and V. Novosad, *APL Mater.*, 2021,**9**,060902

9 F. Vanderveken, J. Mulkers, J. Leliaert, B. Van Waeyenberge, B. Sorée, O. Zografos, F. Ciubotaru and C. Adelmann, *Phys. Rev. B*, 2021, **103**, 054439.

10 R. Chen, C. Chen, L. Han, P. Liu, R. Su, W. Zhu, Y. Zhou, F. Pan and C. Song, *Nat. Commun.*, 2023, **14**, 4427.

11 T. Yokouchi, S. Sugimoto, B. Rana, S. Seki, N. Ogawa, S. Kasai and Y. Otani, *Nat. Nanotechnol.*, 2020, **15**, 361–366.

12 M. Xu, K. Yamamoto, J. Puebla, K. Baumgaertl, B. Rana, K. Miura, H. Takahashi, D. Grundler, S. Maekawa and Y. Otani, *Sci. Adv.*, 2020, **6**, eabb1724.

13 J. Paskauskas, R. Rimeika and D. Ciplys, *J. Phys. Appl. Phys.*, 1995, **28**, 1419.

14 R. Sasaki, Y. Nii and Y. Onose, *Nat. Commun.*, 2021, **12**, 2599.